Communications in Theoretical Physics

Commun. Theor. Phys. **75** (2023) 025303 (11pp) https://doi.org/10.1088/1572-9494/acae80

Probes of axial and nonaxial hexadecapole deformation effects in nuclei around ^{230}U

Zhuo Song[1], **Hua-Lei Wang**[1,*], **Zhen-Zhen Zhang**[1] **and Min-Liang Liu**[2,3]

[1] School of Physics and Microelectronics, Zhengzhou University, Zhengzhou 450001, China
[2] Key Laboratory of High Precision Nuclear Spectroscopy, Institute of Modern Physics, Chinese Academy of Sciences, Lanzhou 730000, China
[3] School of Nuclear Science and Technology, University of Chinese Academy of Sciences, Beijing 100049, China

E-mail: wanghualei@zzu.edu.cn

Received 4 October 2022, revised 2 December 2022
Accepted for publication 27 December 2022
Published 23 February 2023

Abstract

The structure properties for even–even nuclei around ^{230}U, located on the hexadecapole-deformation island, are investigated using the potential-energy-surface calculation within the framework of the macroscopic−microscopic model. The impact of different deformation degrees of freedom (including axial and nonaxial quadrupole and hexadecapole deformations) on total energy, shell, and pairing contributions is analyzed, based on the projected energy maps and curves. The single-particle structure is presented and briefly discussed. To a large extent, a much better agreement with experimental data and other theoretical results is obtained if the hexadecapole deformations, especially the axial one, are taken into account. These results could provide useful insights into understanding the effects of different quadrupole and hexadecapole deformations.

Supplementary material for this article is available online

Keywords: hexadecapole deformation, triaxial deformation, even–even nuclei, potential-energy-surface calculation, macroscopic−microscopic model

(Some figures may appear in colour only in the online journal)

1. Introduction

Nuclear matter space distribution can be approximately described by nuclear shape, which is one of the most important and fundamental physical quantities in nuclear-structure research. Indeed, it is well known that the nuclear shape plays an important role in understanding various nuclear phenomena. Moreover, it is to some extent crucial for understanding the nucleon−nucleon interaction responsible for microscopic nuclear structure. Both the ground state and dynamical properties of nuclei are shape-dependent. In heavy-ion reaction dynamics, the nuclear shape is also revealed to play important roles [1–3]. In practice, the nuclear shape is usually expressed by a set of deformation parameters (e.g. the collective coordinates $\alpha_{\lambda\mu}$ in the expansion of spherical harmonics). The measurements of nuclear shape (namely, such a set of deformation parameters) are of importance for understanding nuclear properties and even checking nuclear structure models. Experimentally, some nuclear deformations are usually determined by scattering measurements (e.g. electron [4], proton [5], neutron [6], deuteron [7], ^{3}He [8], and α scattering [9]), Coulomb excitation [10], heavy ions [11], muonic X-rays [12] and so on. Theoretical estimates usually come from equilibrium deformation predictions given by macroscopic−microscopic Strutinsky-type calculations with phenomenological one-body nuclear potential [e.g. the frequently used Nilsson or Woods−Saxon (WS) potentials] or by microscopic self-consistent Hartree–Fock calculations with effective two-body nucleon−nucleon interactions (e.g. the Skyrme or Gogny nuclear forces). The ground-state shapes have been systematically studied by different methods, cf [13–17].

The lower-order and reflection-symmetric shape degrees of freedom (e.g. $\alpha_{2\mu}$ and $\alpha_{4\mu}$) are expected to be of importance since the other ones only affect a relatively small percentage of all nuclei [18]. Needless to say, the axial

---

[*] Author to whom all correspondence should be addressed.

quadrupole deformation β_2 is the most important and is generally sufficient to explain most nuclear phenomena. It has also been pointed out that some unexpected characteristics, such as wobbling, signature splitting (or inversion), and chiral doublets, may be caused by γ deformation [19–21]. An empirical formula of energy staggering in a γ band was suggested by Zamfir and Casten [22] to indicate the triaxiality in nuclei. In addition, the importance of the hexadecapole deformation β_4 becomes non-negligible in e.g. the rare-earth and actinide regions [23].

Relative to the quadrupole deformation β_2, the hexadecapole deformation is difficult to determine experimentally with good precision, primarily because of its small magnitude [1, 24]. Furthermore, all the results are model dependent and quite different with big uncertainties [25]. However, with the development of techniques and tactical skills, the bottleneck is being or will be broken. For instance, the hexadecapole nuclear deformations have been accurately measured by scattering of α particles at energies well above the Coulomb barrier for rare-earth nuclei [26]. A systematic variation of β_4 from positive in the light rare earths to negative in the heavy ones has been revealed [26] through excitation of the ground rotational band by 50 MeV α particles. The evidence for hexadecapole collectivity in closed-shell nuclei was presented by examining the observed characteristics of the lowest 4^+ excited state [27]. In the lanthanide nuclei, it is found that the β_4 deformation drops from large positive values around $+0.1$ to large negative values around -0.1 as the mass number A increases from 152 to 180 [25]. The β_4 measurements are indeed attracting much interest in research on nuclear shape. Recently, Gupta *et al* [1] determined the hexadecapole β_4 deformation of the light-mass nucleus ^{24}Mg using quasi-elastic scattering measurements.

Very recently, across the whole nuclear chart, we performed a systematic β_4 calculation [28], in which several β_4 deformation islands were found, agreeing with the results in [16] but including the results under rotation. In this study, we mainly focus on the effects of the axial and nonaxial but reflection-symmetric hexadecapole deformation degrees of freedom (e.g. α_{40}, α_{42} and α_{44}) on nuclear structure in the $A = 230$ nuclear region, where the large hexadecapole deformation island was identified both theoretically and experimentally [16, 28]. Prior to the present study, we have investigated axial quadrupole and octupole deformations, triaxial deformation, and the corresponding stiffness in some nuclei [29–35] using potential-energy-surface and total-Routhian-surface calculations, which to a large extent help us to convince ourselves of the validity and correctness of our work.

The paper is organized as follows. In the next section, we summarize the principle of the calculations, with a brief description of the PES method. The results of the calculation and discussion are presented in the section that then follows. The final section gives a brief summary and outlook.

2. Theoretical method

In this section, we recall the unified procedure and give the necessary references on our adopted theoretical method, which are helpful to clarify some details for the general reader (e.g. the various variants of the pairing-energy contribution in the macroscopic−microscopic nuclear-structure models [16, 36]). In this project, we perform the present investigation using the potential-energy-surface method, which is widely used and powerful for studying nuclear structure properties. The usual expression for the total energy reads [cf [37] and references therein]

$$E^{\omega}(Z, N, \hat{\beta}) = E_{\rm LD}(Z, N, \hat{\beta}) + \delta E_{\rm shell}(Z, N, \hat{\beta}) + \delta E_{\rm pair}(Z, N, \hat{\beta}). \qquad (1)$$

The terms $E_{\rm LD}(Z, N, \hat{\beta})$, $\delta E_{\rm shell}(Z, N, \hat{\beta})$ and $\delta E_{\rm pair}(Z, N, \hat{\beta})$ represent the macroscopic liquid-drop energy, the quantum shell correction and the pairing-energy contribution, respectively.

In the literature, the adopted phenomenological liquid-drop (LD) models generally include the standard LD model [38], finite-range droplet model [16], Lublin−Strasbourg drop model [39], and so on. These macroscopic models with slight differences can describe the smoothly varying energy, in which the dominating terms are mainly associated with the volume energy, the surface energy, and the Coulomb energy. In this work, the macroscopic energy is obtained from the standard LD model with the parameters used by Myers and Swiatecki [38, 40]. As mentioned in section V in [40], it needs to be stressed that the potential energy relative to the energy of a spherical liquid drop is adopted in the potential-energy-surface calculations (at this moment, one cannot compare with the binding energy of the nucleus between experiment and theory).

The microscopic energies are calculated based on the single-particle levels which are obtained by solving numerically the Schrödinger equation with a phenomenological one-body mean field or self-consistent one. Here, we adopt the realistic WS Hamiltonian [41], as seen below:

$$H_{\rm WS} = T + V_{\rm cent}(\vec{r}; \hat{\beta}) + V_{\rm so}(\vec{r}, \vec{p}, \vec{s}; \hat{\beta}) + V_{\rm Coul}(\vec{r}, \hat{\beta}), \qquad (2)$$

where the Coulomb potential $V_{\rm Coul}(\vec{r}, \hat{\beta})$, defined as a classical electrostatic potential of a uniformly charged drop, is added for protons. The central part of the WS potential reads

$$V_{\rm cent}(\vec{r}, \hat{\beta}) = \frac{V_0[1 \pm \kappa(N - Z)/(N + Z)]}{1 + \exp[{\rm dist}_{\Sigma}(\vec{r}, \hat{\beta})/a]}, \qquad (3)$$

where the plus and minus signs hold for protons and neutrons, respectively, and the parameter a denotes the diffuseness of the nuclear surface. The term ${\rm dist}_{\Sigma}(\vec{r}, \hat{\beta})$ represents the distance of a point $\vec{r}$ from the nuclear surface Σ parametrized in terms of the multipole expansion of spherical harmonics $Y_{\lambda\mu}(\theta, \phi)$ (which are convenient to describe the geometrical properties), that is,

$$\Sigma\colon R(\theta, \phi) = r_0 A^{1/3} c(\hat{\beta}) \left[1 + \sum_{\lambda} \sum_{\mu=-\lambda}^{+\lambda} \alpha_{\lambda\mu} Y_{\lambda\mu}(\theta, \phi)\right], \qquad (4)$$

where the function $c(\hat{\beta})$ ensures the conservation of the nuclear volume and $\hat{\beta}$ denotes the set of all the deformation parameters. In the present work, the shape parametrization considers quadrupole and hexadecapole degrees of freedom, including nonaxial deformations [that is, $\hat{\beta} \equiv (\alpha_{20}, \alpha_{2\pm2}, \alpha_{40}, \alpha_{4\pm2}, \alpha_{4\pm4})$]. The distance of any point on the nuclear surface from the origin of the coordinate system is denoted by $R(\theta, \phi)$. Generally speaking, the nucleus prefers to possess $x-y$, $y-z$, and $x-z$ plane symmetries. In this case, only the even λ and even μ components are retained. After requesting the hexadecapole degrees of freedom to be functions of the scalars in the quadrupole tensor $\alpha_{2\mu}$, one can reduce the number of independent coefficients to three, namely, β_2, γ, and β_4, which obey the relationships [42]

$$\begin{cases} \alpha_{20} = \beta_2 \cos\gamma \\ \alpha_{22} = \alpha_{2-2} = -\dfrac{1}{\sqrt{2}}\beta_2 \sin\gamma \\ \alpha_{40} = \dfrac{1}{6}\beta_4(5\cos^2\gamma + 1) \\ \alpha_{42} = \alpha_{4-2} = -\dfrac{1}{12}\sqrt{30}\,\beta_4 \sin 2\gamma \\ \alpha_{44} = \alpha_{4-4} = \dfrac{1}{12}\sqrt{70}\,\beta_4 \sin^2\gamma. \end{cases} \tag{5}$$

The (β_2, γ, β_4) parametrization has all the symmetry properties of Bohr's (β_2, γ) parametrization [43, 44]. The spin−orbit potential, which can strongly affect the level order, is defined by

$$V_{\rm so}(\vec{r}, \vec{p}, \vec{s}; \hat{\beta}) = -\lambda\left[\frac{\hbar}{2mc}\right]^2 \times\left\{\nabla\frac{V_0[1 \pm \kappa(N-Z)/(N+Z)]}{1 + \exp[{\rm dist}_{\Sigma_{so}}(\vec{r}, \hat{\beta})/a_{so}]}\right\} \times \vec{p}\cdot\vec{s}, \tag{6}$$

where λ denotes the strength parameter of the effective spin−orbit force acting on the individual nucleons. The new surface Σ_{so} is different from the one in equation (4) due to the different radius parameter. With the WS potential model, one can calculate the WS Hamiltonian matrix by e.g. numerical integral with the aid of a set of orthogonal complete bases. The model parameters (taken from [42, 45]) of the Hamiltonian are usually obtained by the inverse problem theory or χ^2-fitting procedure (e.g. fitting the experimental single-particle levels) and can often be adopted for the present mass region (e.g. cf [17]). In this work, we use the eigenfunctions of the axially deformed harmonic oscillator potential in the cylindrical coordinate system as the basis function, as seen below:

$$|n_\rho n_z \Lambda\Sigma\rangle = \psi^{\Lambda}_{n_\rho}(\rho)\psi_{n_z}(z)\psi_{\Lambda}(\varphi)\chi(\Sigma). \tag{7}$$

For more details, one can see e.g. [46]. During the calculation, the eigenfunctions with the principal quantum numbers $N \leqslant 12$ and 14 are chosen as the basis set for protons and neutrons, respectively. It is found that, via such a basis cutoff, the results are sufficiently stable with respect to a possible enlargement of the basis space, indicating the completeness to some extent. In addition, the time reversal (resulting in the Kramers degeneracy) and spatial symmetries (e.g. the existence of three symmetry planes mentioned above) are used for simplifying the calculations of the Hamiltonian matrix.

The shell correction $\delta E_{\rm shell}(Z, N, \hat{\beta})$, as seen in equation (1), which is usually the most important correction to the LD energy, can be calculated by the Strutinsky method,

$$\delta E_{\rm shell}(Z, N, \hat{\beta}) = \sum e_i - \int e\tilde{g}(e){\rm d}e, \tag{8}$$

where e_i denotes the calculated single-particle levels and $\tilde{g}(e)$ is the so-called smooth level density. Obviously, the smooth level distribution function is the most important quantity, which was earlier defined as

$$\tilde{g}(e, \gamma) \equiv \frac{1}{\gamma\sqrt{\pi}}\sum_i \exp\left[-\frac{(e-e_i)^2}{\gamma^2}\right], \tag{9}$$

where γ denotes the smoothing parameter without much physical significance. To eliminate any possibly strong γ-parameter dependence for the calculated result, the mathematical form of the smooth level density $\tilde{g}(e)$ is optimized by introducing a phenomenological curvature-correction polynomial $P_p(x)$ [40, 47–49],

$$\tilde{g}(e, \gamma, p) = \frac{1}{\gamma\sqrt{\pi}}\sum_{i=1} P_p\left(\frac{e-e_i}{\gamma}\right) \times\exp\left[-\frac{(e-e_i)^2}{\gamma^2}\right]. \tag{10}$$

The corrective polynomial $P_p(x)$ can be expanded in terms of the Hermite or Laguerre polynomials. The corresponding coefficients of the expansion can be obtained using the orthogonality properties of these polynomials and the Strutinsky condition [50]. So far, some other methods have also been developed for calculating microscopic shell correction, e.g. the semiclassical Wigner−Kirkwood expansion method [42, 51] and the Green function method [52]. In this work, we adopt the widely used Strutinsky method despite its known problems that appear for mean-field potentials of finite depth as well as for nuclei close to the proton or neutron drip lines. The smooth level density is calculated with a sixth-order Hermite polynomial and a smoothing parameter $\gamma = 1.20\hbar\omega_0$, where $\hbar\omega_0 = 41/A^{1/3}$ MeV [40].

Another important single-particle correction, besides the shell correction, is the pairing-energy contribution. As is well known, because of the short-range interaction of nucleon pairs in time-reversed orbitals, the total potential energy relative to the energy without pairing in a nucleus is always reduced. There exist various variants of the pairing-energy contribution in microscopic-energy calculations, as was recently pointed out in [53]. Typically, several kinds of phenomenological pairing energy expressions (namely, pairing correlation and pairing correction energies employing or not employing the particle number projection technique) are widely adopted in applications of the macroscopic−microscopic approach [53]. In the present work, the contribution $\delta E_{\rm pair}(Z, N, \hat{\beta})$ in equation (1) is the pairing correlation energy. The pairing is treated by the Lipkin−Nogami (LN) method [54], which helps avoid not only the spurious pairing phase transition but also the particle number fluctuation encountered in the simpler BCS calculation. In the LN technique [54, 55], it aims to minimize the expectation value of the following model Hamiltonian:

$$\hat{\mathcal{H}} = \hat{H}_{\rm WS} + \hat{H}_{\rm pair} - \lambda_1\hat{N} - \lambda_2\hat{N}^2. \tag{11}$$

Here, $\hat{H}_{\rm pair}$ indicates the pairing interaction Hamiltonian [56, 57]. The pairing strength is determined by the average gap method [57]. The pairing window, including dozens of single-particle levels, and the respective states (e.g. half of the particle number Z or N) just below and above the Fermi energy, is adopted empirically for both protons and neutrons. The pairing gap Δ, Fermi energy λ [namely, $\lambda_1 + 2\lambda_2(N_{\text{total}} + 1)$], particle number fluctuation constant λ_2, occupation amplitudes v_k, and shifted single-particle energies ε_k can be determined from the following $2(N_2 - N_1) + 5$ coupled nonlinear equations [54, 57]:

$$\begin{cases} N_{\text{total}} = 2\sum_{k=N_1}^{N_2} v_k^2 + 2(N_1 - 1), \\ \Delta = G\sum_{k=N_1}^{N_2} u_k v_k, \\ v_k^2 = \dfrac{1}{2}\left[1 - \dfrac{\varepsilon_k - \lambda}{\sqrt{(\varepsilon_k - \lambda)^2 + \Delta^2}}\right], \\ \varepsilon_k = e_k + (4\lambda - G)v_k^2, \\ \lambda_2 = \dfrac{G}{4}\left[\dfrac{\left(\sum_{k=N_1}^{N_2} u_k^3 v_k\right)\left(\sum_{k=N_1}^{N_2} u_k v_k^3\right) - \sum_{k=N_1}^{N_2} u_k^4 v_k^4}{\left(\sum_{k=N_1}^{N_2} u_k^2 v_k^2\right)^2 - \sum_{k=N_1}^{N_2} u_k^4 v_k^4}\right], \end{cases} \tag{12}$$

where $u_k^2 = 1 - v_k^2$ and $k = N_1, N_1 + 1, \cdots, N_2$. The LN pairing energy for the system of even–even nuclei at the 'paired solution' (pairing gap $\Delta \neq 0$) is given by [16, 54]

$$E_{\text{LN}} = \sum_k 2{v_k}^2 e_k - \frac{\Delta^2}{G} - G\sum_k {v_k}^4 - 4\lambda_2 \sum_k {u_k}^2 {v_k}^2, \tag{13}$$

where ${v_k}^2$, e_k, Δ and λ_2 represent the occupation probabilities, single-particle energies, pairing gap and number-fluctuation constant, respectively. Correspondingly, the partner expression at the 'no-pairing solution' ($\Delta = 0$) reads

$$E_{\text{LN}}(\Delta = 0) = \sum_k 2e_k - G\frac{N}{2}. \tag{14}$$

The pairing correlation is defined as the difference between paired solution E_{LN} and no-pairing solution $E_{\text{LN}}(\Delta = 0)$.

As mentioned in [58], after performing the several standard steps, the total energy can be obtained at each sampling deformation grid. Further, the smooth potential-energy surface/map is able to be given with the help of the interpolation techniques, e.g. a cubic spline function, and then the equilibrium deformations and other physical quantities at such a shape can be determined. Note that different parametrizations generate similar equilibrium deformations in the stiff nuclei. In the soft nuclei, the so-called equilibrium deformations, which may sensitively depend on the model parameters, are meaningless and the dynamic deformations should, in principle, be taken into account.

3. Results and discussion

The calculation of the potential-energy surface is very helpful for understanding the structure properties from different deformation degrees of freedom in nuclei. We perform realistic total energy calculations using the deformed WS mean-field Hamiltonian in the deformation spaces (β_2, γ, $\alpha_{4\mu=0,2,4}$) and (β_2, γ, β_4). As examples, in figure 1, the results of potential energy surfaces projected on the (X, Y) and (β_2, γ) planes are illustrated for ${}^{230}_{92}\text{U}_{138}$. Similarly projected maps are widely used in the literature. In figure 1(a), the usual Cartesian quadrupole coordinates ($X = \beta_2 \sin(\gamma + 30°)$, $Y = \beta_2 \cos(\gamma + 30°)$) are used. In figure 1(b), the β_2 and γ deformation variables are directly presented as the horizontal and vertical coordinates in a Cartesian coordinate system, instead of the (β_2, γ) plane in the polar coordinate system. For the static energy surfaces, the γ domain [$-60°$, $60°$] is adopted to guide the eyes, though, in principle, half is enough. These two maps are equivalent but the latter can display the triaxial effect better, especially at the weak β_2 deformation. In figure 1, the minima with $E = -1.8278$ MeV are located at $\beta_2 = 0.38$ and $\gamma = \pm 30°$. It should be pointed out that, in these two testing figures, the hexadecapole deformation degree of freedom is set to zero and, for display purposes, the energies at each map are respectively normalized to their minima. Obviously, such a simple calculation is not in agreement with the fact (e.g. experimental $\beta_2 = 0.26$ [59]). Generally, an extended deformation subspace, including the hexadecapole deformation, is necessary.

Figure 2 illustrates the potential energies projected on the (β_2, γ) planes with the consideration of different hexadecapole deformation degrees of freedom. For instance, in figures 2(a)–(d), the energy minimization is respectively performed over α_{40}, α_{42}, α_{44} and β_4 at each deformation grid (β_2, γ). One can see that the α_{40} deformation may result in a large decrease in energy. Calculations show the occurrence of non-zero triaxial minima after considering α_{42} and α_{44} deformations, as seen in figures 2(b) and (c). Not only the positions but also the shapes of the potential-energy surface near the minima are different, indicating the different effects on nuclear structure. To synthetically consider the different hexadecapole deformation degrees of freedom, we show the map of minimized energy over β_4, according to the relationship e.g. in equation (5). However, the present results show that the different local minima may coexist depending on the selected deformation space. In fact, the full space expanded by the spherical harmonics, as seen in equation (4), is infinite in principle. The complexity of the nuclear shape is similar (or even equivalent) to the nuclear interaction. Reasonable selection of the deformation subspace in different mass regions and/or different spin and excitation conditions is worth exploring depending on experiences.

In order to understand how dependent the calculated total energies are on these hexadecapole deformations $\alpha_{4\mu=0,2,4}$, figure 3 illustrates the corresponding 2D maps for ${}^{230}_{92}\text{U}_{138}$ projected on the (β_2, $\alpha_{4\mu=0,2,4}$) and (β_2, β_4) planes (we focus on the even-μ components presently). To separately investigate the effects of different hexadecapole deformation parameters on the energy surfaces, in the left four subfigures of figure 3, we perform the calculations in 2D deformation spaces displayed by the horizontal and vertical coordinates, ignoring other degrees of freedom. It needs to be stressed that the hexadecapole deformation β_4 involves the fixed

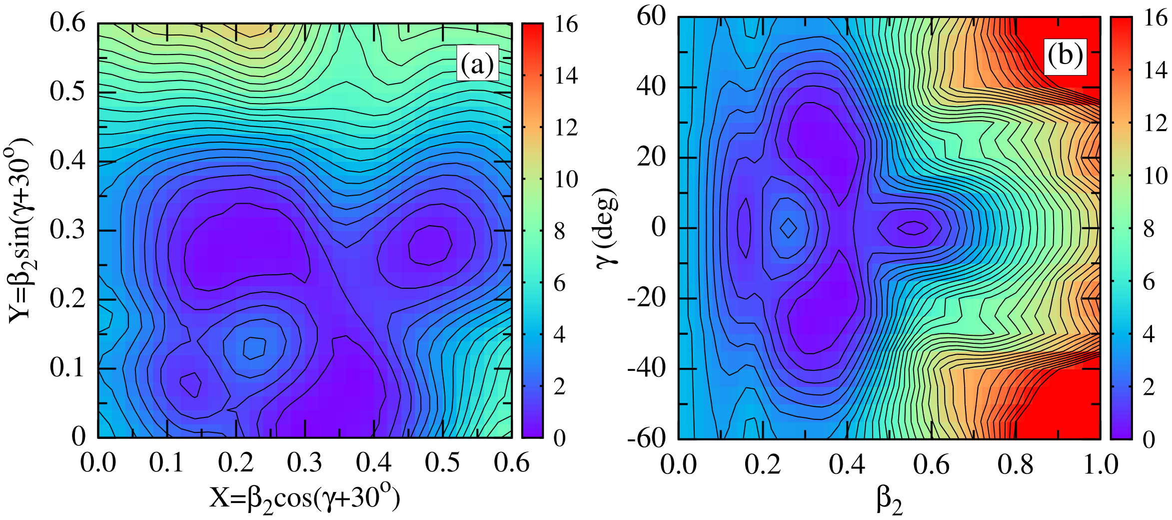

Figure 1. Projections of calculated total energy on the (X, Y) (a) and (β_2, γ) (b) planes for $^{230}_{92}U_{138}$. The energy interval between neighboring contour lines is 0.5 MeV. See the text for more details.

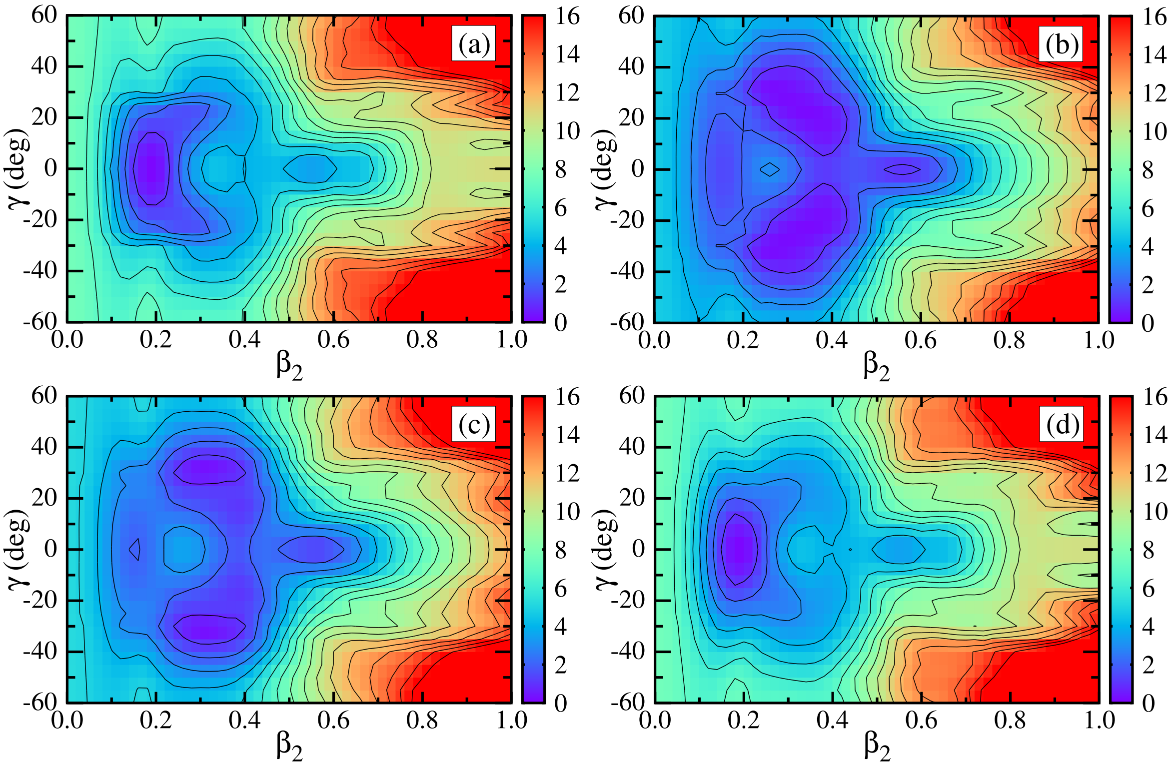

Figure 2. Similar to figure 1(b) but the energy minimization was respectively performed over the hexadecapole deformation degrees of freedom α_{40}, α_{42}, α_{44} and β_4 in (a), (b), (c) and (d); and the energy minimum (in MeV) and equilibrium deformations (E_{min}; β_2, γ, $\alpha_{4\mu=0,2,4}$ or β_4) are respectively (−5.2731; 0.20, 0°, −0.03), (−2.3548; 0.26, 30°, 0.01), (−2.9026; 0.32, 30°, 0.06) and (−5.2421; 0.20, 0°, −0.03). The energy interval between two contour lines is 1 MeV.

relationships of $\{\alpha_{4\mu=0,2,4}\}$ and γ, as mentioned above. For instance, three deformation parameters $\{\alpha_{4\mu=0,2,4}\}$ can be determined in terms of a pair of given β_2 and γ values. It can be seen from the left panel of figure 3 that the α_{40} (equivalently β_4 at $\gamma = 0°$) deformation plays an important role in changing the energy minima, similar to the case in figure 2. The deformation spaces including the non-axial deformation parameters α_{42} and α_{44} can generate three energy minima but the energies are higher than that in the (β_2, α_{40}) plane. In the right part, at each deformation point of the corresponding map, the minimization is performed over triaxial deformation γ. Indeed, one can find that non-zero $\{\alpha_{4\mu=0,2,4}\}$ values appear at the minimum position, indicating that the three $\{\alpha_{4\mu=0,2,4}\}$ deformations play a role during the calculations; see e.g. figures 3(e)–(g). For simplicity of calculation and simultaneously including the effects of three such hexadecapole deformation parameters, the total energy projection on the (β_2, β_4) plane is illustrated in figure 3(h), minimized over

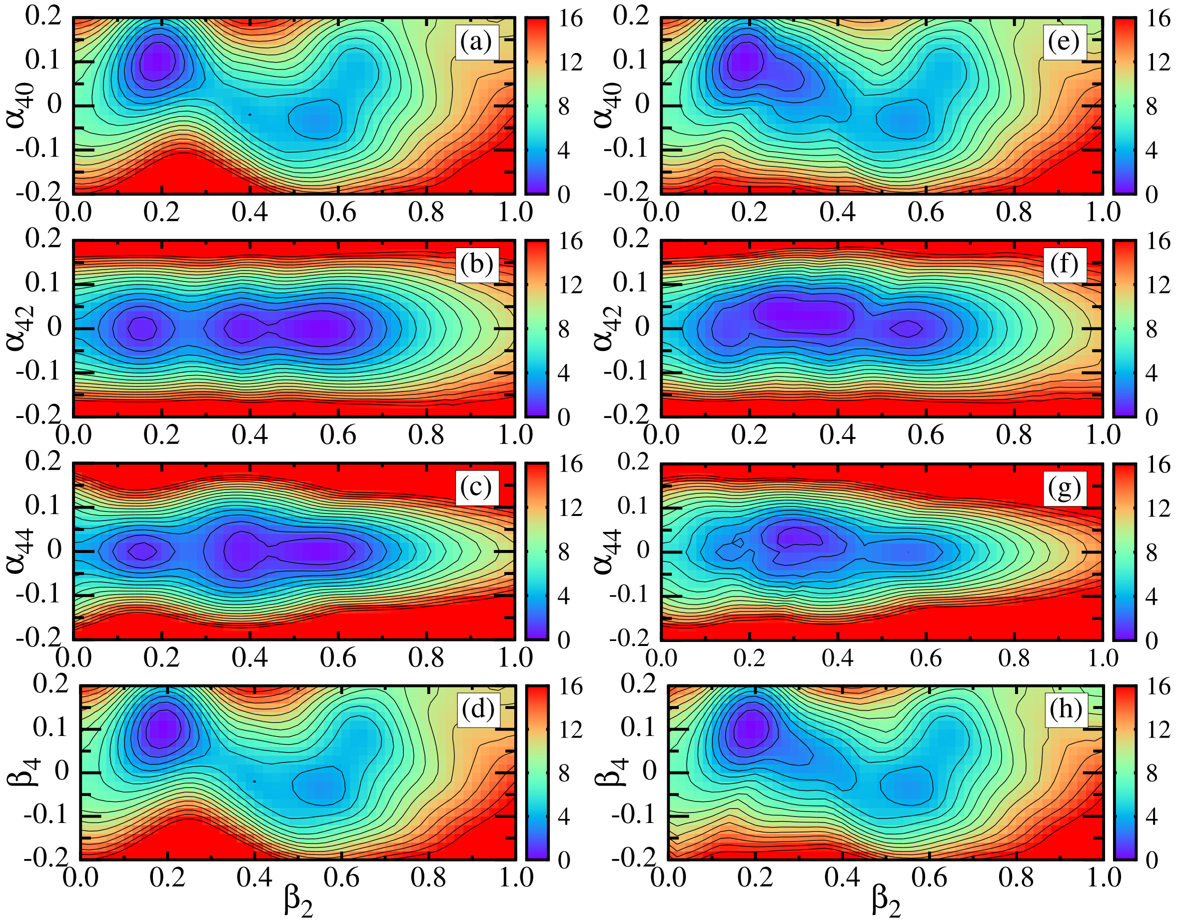

Figure 3. Similar to figure 2 but projections on the (β_2,α_{40}), (β_2,α_{42}), (β_2,α_{44}) and (β_2,β_4) planes for $^{230}_{92}$U$_{138}$. In the (a), (b), (c) and (d) subplots, the triaxial deformation γ was set to zero during the calculations and the energy minimum (in MeV) and equilibrium deformations ($E_{\rm min}$; β_2, $\alpha_{4\mu=0,2,4}$ or β_4) are respectively (−5.2041; 0.20, 0.10), (−1.5279; 0.56, 0.00), (−1.5279; 0.56, 0.00) and (−5.2041; 0.20, 0.10). In the right four subfigures (e), (f), (g) and (h), the minimization was performed over γ at each mesh grid and, similarly, the values ($E_{\rm min}$; β_2, γ, $\alpha_{4\mu=0,2,4}$ or β_4) are respectively (−5.2041; 0.20, 0°, 0.10), (−2.3059; 0.26, 34°, 0.04), (−3.5264; 0.28, 32°, 0.02) and (−5.2041; 0.20, 0°, 0.10).

γ. In the following investigation, the hexadecapole deformation β_4 parameter is selected, which can give the collective coordinates $\{\alpha_{4\mu=0,2,4}\}$ by combining the γ parameter. Similar to the γ deformation, the β_4 deformation has an obvious influence on the energy minimum for this nucleus, resulting in a strong energy reduction at the first minimum.

In figure 4, we provide further evolution information on the total energy and its different components in functions of the quadrupole deformation β_2 for $^{230}_{92}$U$_{138}$, primarily aiming to show the impact of triaxial γ and hexadecapole β_4 deformations on these energies. In the left panel, subfigures (a)–(d) represent the total energy, together with the macroscopic LD energy $E_{\rm ld}$, shell correction $\delta E_{\rm shell}$ and pairing correlation $\delta E_{\rm pair}$, in functions of β_2 at three selected γ values. For simplicity, other deformation degrees of freedom are ignored. One can see that the macroscopic LD energies slightly increase with increasing triaxial deformation γ at relatively large β_2 deformation (e.g. after $\beta_2 = 0.6$). For $\beta_2 < 0.4$, the changed γ deformations have almost nothing to do with the LD energies. The shell corrections exhibit a large staggering both with changing β_2 and γ, leading to similar trends in the corresponding total energies. The differences in total energies at the three γ values are mainly from shell corrections; see e.g. figure 4(c). Both the LD energy and pairing correlation have small effects with changing β_2 and γ. Similarly, in the right part, e.g. from figure 4(e) to figure 4(h), the results are illustrated at three selected β_4 deformation values. The β_4 deformation mainly affects the microscopic shell effect. For the macroscopic energies, it seems that a critical point $\beta_2 \simeq 0.55$ exists. Before (after) this point, the LD energies increase (decrease) with increasing β_4. In addition, it can be noticed (cf table 1) that the inclusion of the β_4 deformation is critical to reproducing the experimental β_2 value and/or other theoretical results.

In the pairing-energy calculation, both the pairing model and the pairing strength are critical and controversial. A detailed discussion of these aspects is beyond the scope of the present work (we refer the interested readers to e.g. [57]). Here, in figure 5, we illustrate the impacts of the adjustments to the pairing strength on pairing contributions and total energies. As mentioned in [60], for the selected pairing model, the pairing strength G ($\equiv FG_0$) can be adjusted by comparing the theoretical pairing gap with experimental data. It seems from figure 5 that the pairing strength continuously

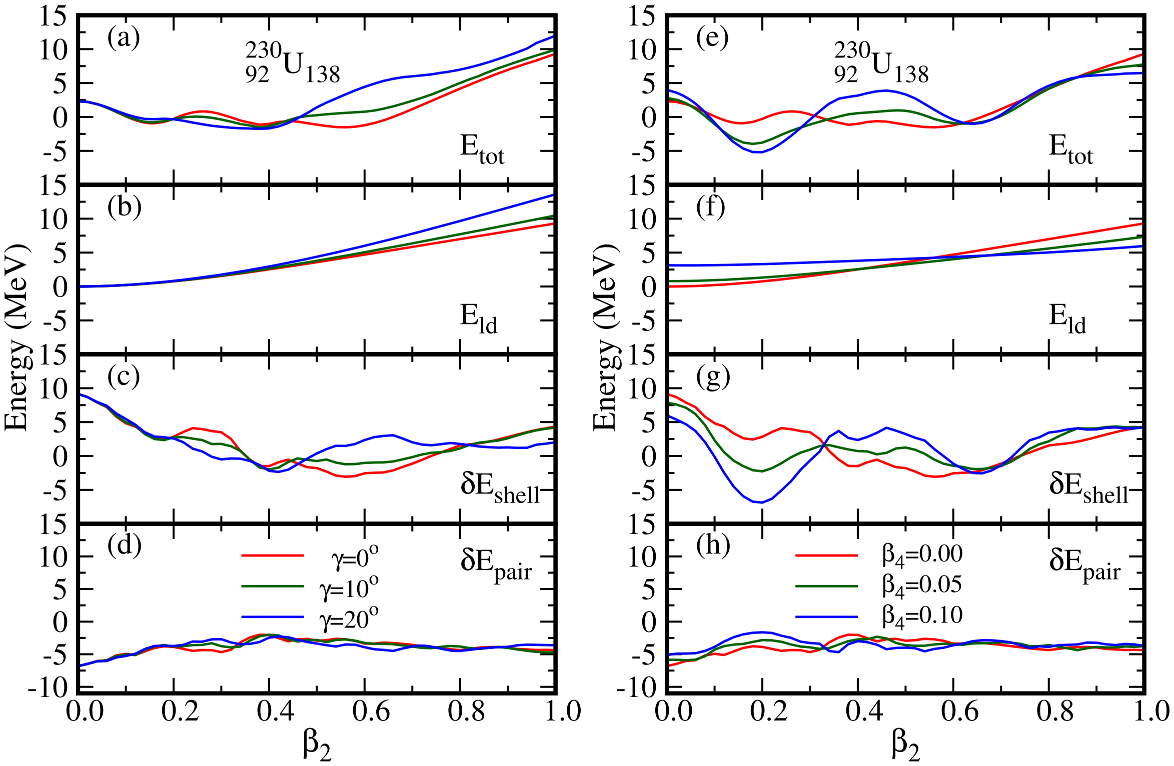

Figure 4. Left: Calculated total-energy E_{tot} (a) curves against the quadrupole deformation β_2 at three cases $\gamma = 0^\circ, 10^\circ$ and 20°, together with its macroscopic component E_{ld} (b), microscopic shell correction $\delta E_{\mathrm{shell}}$ (c) and pairing-energy contribution δE_{pair} (d), for the nucleus $^{230}_{92}\mathrm{U}_{138}$. Other deformation parameters are ignored. Right: Similar to the left but with the corresponding three energy curves respectively plotted at $\beta_4 = 0.00$, 0.05 and 0.10.

Table 1. Calculated results (PES) for ground-state equilibrium deformation parameters β_2 and β_4 for even–even $^{226-230}$Th,$^{228-232}$U and $^{230-234}$Pu, together with the FY+FRDM(FF) [62], HFBCS [63], and ETFSI [64] calculations and partial experimental (Exp.) β_2 values [59] for comparison.

Nuclei	β_2					β_4			
	PES[a]	FF	HFBCS	ETFSI	Exp.[b]	PES	FF	HFBCS	ETFSI
$^{226}_{90}\mathrm{Th}_{136}$	0.160	0.173	0.20	0.17	0.230	0.096	0.111	0.04	0.08
$^{228}_{90}\mathrm{Th}_{138}$	0.174	0.182	0.21	0.19	0.230	0.098	0.112	0.04	0.08
$^{230}_{90}\mathrm{Th}_{140}$	0.185	0.198	0.21	0.19	0.246	0.099	0.115	0.04	0.08
$^{228}_{92}\mathrm{U}_{136}$	0.177	0.191	0.21	0.19	—	0.103	0.114	0.04	0.09
$^{230}_{92}\mathrm{U}_{138}$	0.191	0.199	0.21	0.19	0.260	0.105	0.115	0.04	0.09
$^{232}_{92}\mathrm{U}_{140}$	0.200	0.207	0.22	0.21	0.264	0.102	0.117	0.03	0.08
$^{230}_{94}\mathrm{Pu}_{136}$	0.189	0.198	0.25	0.19	—	0.098	0.115	0.03	0.09
$^{232}_{94}\mathrm{Pu}_{138}$	0.200	0.208	0.25	0.21	—	0.098	0.117	0.03	0.08
$^{234}_{94}\mathrm{Pu}_{140}$	0.208	0.216	0.25	0.22	—	0.094	0.109	0.03	0.07

[a] The calculated ground-state $|\gamma|$ values of these nuclei are less than 2°.

[b] The uncertainties for deduced β_2 values are no more than 0.011; see [59] for details.

affects the pairing correlation, translating the energy curves. The negative δE_{pair} originates from short-range attractions of paired nucleons (as expected, the larger the factor F is, the stronger the attraction).

In functions of β_2 and β_4, figure 6 illustrates the calculated proton and neutron single-particle levels (near the Fermi levels) which correspond to the eigenstates of the one-body WS Hamiltonian. Usually, a set of conserved quantum numbers (associated with a complete set of commuting observables) are used for labeling the corresponding single-particle levels and wave functions. In the spherical case, for instance, the quantum numbers n, l and j, corresponding to the principal quantum number, the orbital angular momentum, and the total angular momentum, respectively, are adopted. Similar to atomic spectroscopy, the notations $s, p, d, f, g, h \cdots$ are used for $l = 0$, 1, 2, 3, 4, 5 $\cdots$, respectively. Due to the strong spin–orbit coupling, the single particle level with l splits into two levels with $j = l \pm 1/2$, which has $2j + 1$

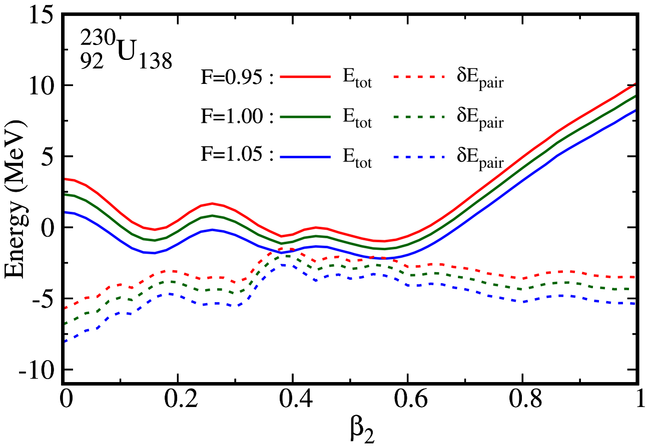

Figure 5. Total energy and pairing correlation curves against the quadrupole deformation β_2 at the pairing-strength factor $F = 0.95$, 1.00 and 1.05 for ${}^{230}_{92}\mathrm{U}_{138}$.

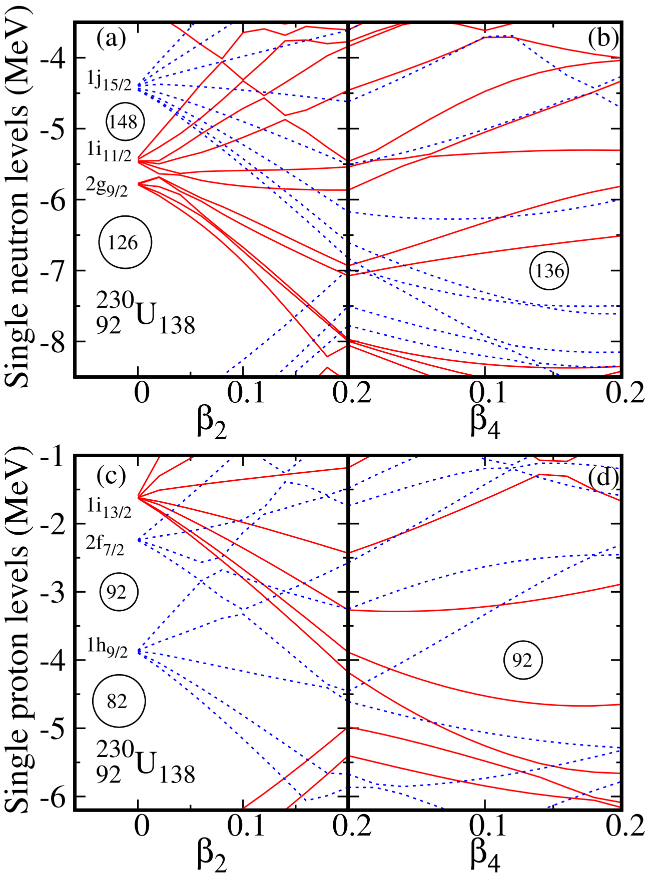

Figure 6. Calculated neutron (top) and proton (bottom) single-particle energies as functions of the quadrupole deformation β_2 (left) and hexadecapole deformation β_4 for ${}^{230}_{92}\mathrm{U}_{138}$, focusing on the domain near the Fermi surface. The levels with positive and negative parities are respectively denoted by red solid and blue dotted lines. Spherical single-particle orbitals (i.e., at $\beta_2 = 0.0$) in the window of interest are labeled by the quantum numbers *nlj*.

degenerate states. From figure 6, one can see that the spherical shell gaps, e.g. $Z = 82$ and $N = 126$, are reproduced at $\beta_2 = 0.0$. Once the deformed shape occurs, the $2j + 1$ degeneracy is broken and the level labeled by *nlj* splits into $j + 1/2$ components. Each component (level) is typically double degenerate, due to Kramers degeneracy. The asymptotic Nilsson quantum numbers $\Omega^{\pi}[Nn_z\Lambda]$ are often used for describing the deformed single-particle level. Here, note that N is the total oscillator shell quantum number; n_z stands for the number of oscillator quanta in the z direction (the direction of the symmetry axis); Λ is the projection of angular momentum along the symmetry axis; Σ is the projection of intrinsic spin along the symmetry axis; Ω is the projection of total angular momentum j (including orbital l and spin s) on the symmetry axis; and $\Omega = \Lambda + \Sigma$. It should be pointed out that the virtual crossing removal [61] of single-particle levels with the same symmetries in these plots is not performed but this does not affect the identification of the single-particle levels. From this figure, it can be found that the β_4 deformation plays a critical role during the shell evolution. For example, the shell gap does not appear at $\beta_2 \approx 0.20$ near the Fermi surface for either protons or neutrons. However, the energy gaps clearly appear at e.g. $\beta_4 \approx 0.10$, in good agreement with the following calculations (e.g. cf table 1).

Table 1 illustrates the calculated quadrupole deformation β_2 and hexadecapole deformation β_4 for nine even–even nuclei on the selected β_4 deformation island, together with the available experimental data [59] and/or other accepted theories for comparison. As seen in this table, other theoretical calculations include the results given by the fold-Yukawa (FY) single-particle potential and the finite-range droplet model (FRDM) [62], the Hartree–Fock-BCS (HFBCS) [63] and the extended Thomas−Fermi plus Strutinsky integral (ETFSI) methods [64]. One can find that all the theoretical results underestimate the data. These theoretical values are somewhat model-dependent but in basic agreement with each other. Relatively, the HFBCS calculation gives the largest β_2 but the smallest β_4 values. Our calculated β_2 deformations are slightly smaller than the FF and ETFSI calculations. As discussed by Dudek *et al* [65], the underestimated quadrupole deformation β_2 should be slightly modified by the empirical relationship $1.10\beta_2$-$0.03(\beta_2)^3$ in the WS-type mean-field calculations. Nevertheless, the β_4 values lie between the FF and ETFSI calculations. It should be noted that the dynamical effects (e.g. the vibrating coupling) may to some extent be responsible for the underestimations of β_2 values (the data extracted from $BE(2)$ automatically include the vibrating effect, e.g. see [58] and references therein), especially in the soft nuclei.

To exhibit the depth and softness properties of the minimum near the equilibrium shape, we show four types of total energy curves in functions of β_2 for nine selected nuclei ${}^{226,228,230}\mathrm{Th}$, ${}^{228,230,232}\mathrm{U}$ and ${}^{230,232,234}\mathrm{Pu}$ in figure 7. Note that the blue, red, green, and black lines respectively correspond to those curves whose energies are minimized over γ and β_4; β_4; γ; and none. One can notice that the nuclear shapes are very soft and several coexisting shapes may be produced if just considering the triaxial deformation degree of freedom. The inclusion of the triaxial γ deformation leads to the disappearance of the barrier between $\beta_2 \sim 0.2$ and 0.3, even producing an energy pocket (e.g. see the green lines in ${}^{232}\mathrm{U}$ and ${}^{232,234}\mathrm{Pu}$). In addition, it seems that the

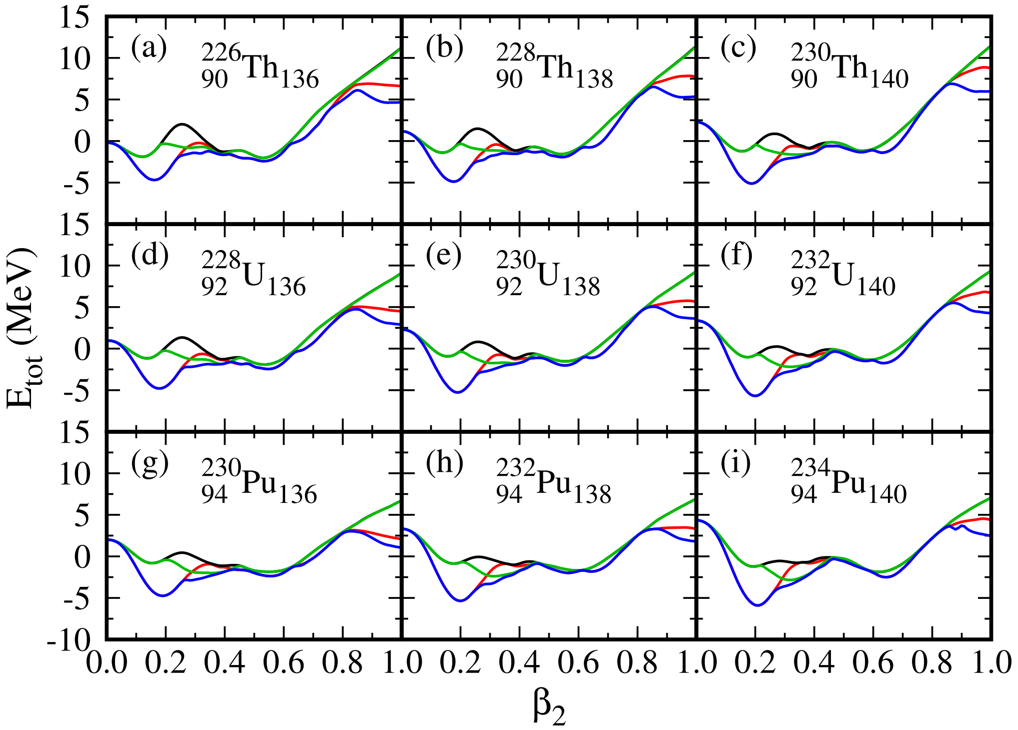

Figure 7. Four types of deformation energy curves as the function of quadrupole axial deformation β_2 for nine nuclei ^{226,228,230}Th, ^{228,230,232}U and ^{230,232,234}Pu. The lines with different colors denote whether or not the total energy at each β_2 was minimized and, if so, with respect to what deformation parameter(s). For instance, at each β_2 point of the green line, the minimization was performed over γ (blue, over γ and β_4; red, over β_4; and black, over none). Note that the black and blue curves always occupy the highest and lowest positions, respectively, though they may be not displayed fully due to the strong overlap with other ones.

hexadecapole deformation β_4 plays a critical role in reproducing the comparable values with data and/or previous theories. The minima e.g. between $\beta_2 = 0.1$ and 0.2 are reduced by 4−5 MeV and, simultaneously, the equilibrium β_2 deformations of the minima increase owing to the β_4 effects. In the large deformed region (e.g. $\beta > 0.8$), both the β_4 and β_4-induced γ deformations (without β_4, the γ deformation does not work, e.g. see the overlapped green and black lines) decrease the outer barriers. In previous studies [33, 66], it was pointed out that the triaxial γ and octupole deformation β_3 could reduce the outer barriers. To explore a more reasonable deformation subspace, especially near the outer barrier, it may be necessary to simultaneously consider, at least, the triaxial, octupole, and hexadecapole correlations.

4. Summary

In summary, we have investigated the effects of the axial and nonaxial quadrupole and hexadecapole deformations on potential energy surfaces of nuclei on the β_4 island (around ^{230}U) within macroscopic−microscopic frameworks. The calculations are performed in multidimensional (β_2, γ, β_4) and (β_2, γ, $\alpha_{4\mu}$) deformation spaces. It is found that the hexadecapole deformations strongly modify the nuclear potential landscapes in these nuclei. Near the equilibrium energy pocket, the hexadecapole deformation β_4 can decrease the minimum by 4–5 MeV. In the large deformed region, the β_4 deformation has an important influence on the outer barrier and, even during the evolution process from the first minimum to the strongly elongated β_2 region, still plays a certain role. The hexadecapole deformations are critical degrees of freedom in research on the nuclear equilibrium shape and fission process. Both experimentally and theoretically, it is to an extent meaningful to further study the hexadecapole deformations in nuclei.

Acknowledgments

This work was supported by the National Natural Science Foundation of China (No. 11975209, No. U2032211, and No. 12075287), the Physics Research and Development Program of Zhengzhou University (No. 32410017), the Project of Youth Backbone Teachers of Colleges and Universities of Henan Province (No. 2017GGJS008). Some of the calculations were conducted at the National Supercomputing Center in Zhengzhou.

Conflict of interest

The authors declare that they have no known competing financial interests or personal relationships that could have appeared to influence the work reported in this paper.

References

[1] Gupta Y K *et al* 2020 Determination of hexadecapole (β_4) deformation of the light-mass nucleus ^{24}Mg using quasi-elastic scattering measurements *Phys. Lett.* B **806** 135473

[2] Hagino K and Takigawa N 2012 Subbarrier fusion reactions and many-particle quantum tunneling *Prog. Theor. Phys.* **128** 1061–106

[3] Bao X J, Guo S Q, Zhang H F and Li J Q 2016 Influence of hexadecapole deformation on production cross sections of superheavy nuclei *J. Phys. G: Nucl. Part. Phys.* **43** 125105

[4] Cooper T, Bertozzi W, Heisenberg J, Kowalski S, Turchinetz W, Williamson C, Cardman L, Fivozinsky S, Lightbody J Jr and Penner S 1976 Shapes of deformed nuclei as determined by electron scattering: ^{152}Sm, ^{154}Sm, ^{166}Er, ^{176}Yb, ^{232}Th, and ^{238}U *Phys. Rev.* C **13** 1083–94

[5] Fabrici E, Micheletti S, Pignanelli M, Resmini F G, Leo R D, D'Erasmo G and Pantaleo A 1980 Proton elastic scattering on light nuclei. II. Nuclear structure effects *Phys. Rev.* C **21** 844–60

[6] Haouat G, Lagrange C, de Swiniarski R, Dietrich F, Delaroche J P and Patin Y 1984 Nuclear deformations of ^{24}Mg, ^{28}Si, and ^{32}S from fast neutron scattering *Phys. Rev.* C **30** 1795–809

[7] Kiss A, Aspelund O, Hrehuss G, Knöpfle K T, Rogge M, Schwinn U, Seres Z, Turek P and Mayer-Böricke C 1976 The (d, d) and (d, d′) scattering on ^{24}Mg at energies between 60 and 90 MeV *Nucl. Phys.* A **262** 1–18

[8] Peterson R J and Cecil F E 1978 Isoscalar excitations of ^{24}Mg by inelastic ^{3}He scattering *Nucl. Phys.* A **297** 10–34

[9] Rebel H, Schweimer G W, Schatz G, Specht J, Löhken R, Hauser G, Habs D and Klewe-Nebenius H 1972 Quadrupole and hexadecapole deformation of 2s-1d shell nuclei *Nucl. Phys.* A **182** 145–73

[10] Wollersheim H J, Wilcke W and Elze T W 1975 E2 and E4 transition moments in ^{172}Yb, ^{174}Yb, and ^{176}Yb *Phys. Rev.* C **11** 2008–11

[11] Siwek-Wilczyńska K, Wilczyńsk J and Christensen P R 1974 Elastic and inelastic scattering in the ^{16}O + ^{24}Mg system *Nucl. Phys.* A **229** 461–70

[12] Powers R J *et al* 1975 Precise determination of E2 and E4 moments in ^{165}Ho from muonic X rays *Phys. Rev. Lett.* **34** 492–5

[13] Möller P, Sierk A J, Ichikawa T and Sagawa H 2016 Nuclear ground-state masses and deformations: FRDM(2012) *At. Data Nucl. Data Tables* **109−110** 1–204

[14] Goriely S, Tondeur F and Pearson J M 2001 A Hartree−Fock nuclear mass table *At. Data Nucl. Data Tables* **77** 311–81

[15] Aboussir Y, Pearson J M, Dutta A K and Tondeur F 1995 Nuclear mass formula via an approximation to the Hartree −Fock method *At. Data Nucl. Data Tables* **61** 127–76

[16] Möller P, Nix J R, Myers W D and Swiatecki W J 1995 Nuclear ground-state masses and deformations *At. Data Nucl. Data Tables* **59** 185

[17] Wu Z Y, Qi C, Wyss R and Liu H L 2015 Global calculations of microscopic energies and nuclear deformations: Isospin dependence of the spin−orbit coupling *Phys. Rev.* C **92** 024306

[18] Möller P, Sierk A J, Bengtsson R, Sagawa H and Ichikawa T 2009 Global calculation of nuclear shape isomers *Phys. Rev. Lett.* **103** 212501

[19] Bengtsson R, Frisk H, May F R and Pinston J A 1984 Signature inversion − A fingerprint of triaxiality *Nucl. Phys.* A **415** 189–214

[20] Ødegård S W *et al* 2001 Evidence for the wobbling mode in nuclei *Phys. Rev. Lett.* **86** 5866–9

[21] Starosta K *et al* 2001 Evidence for the wobbling mode in nuclei *Phys. Rev. Lett.* **86** 971–4

[22] Zamfir N V and Casten R F 1991 Signatures of γ softness or triaxiality in low energy nuclear spectra *Phys. Lett.* B **260** 265–70

[23] Hendrie D I 1973 Comparison of nuclear and Coulomb measurements of nuclear shapes *Phys. Rev. Lett.* **31** 478–81

[24] Gupta R K, Manhas M and Greiner W 2006 Compactness of the ^{48}Ca induced hot fusion reactions and the magnitudes of quadrupole and hexadecapole deformations *Phys. Rev.* C **73** 054307

[25] Jia H M *et al* 2014 Extracting the hexadecapole deformation from backward quasi-elastic scattering *Phys. Rev.* C **90** 031601(R)

[26] Hendrie D L, Glendenning N K, Harvey B G, Jarvis O N, Duhm H H, Saudinos J and Mahoney J 1968 Determination of Y_{40} and Y_{60} components in the shapes of rare earth nuclei *Phys. Lett.* B **26** 127–30

[27] Sood P C, Sheline R K and Singh B 1995 Evidence for hexadecapole collectivity in closed-shell nuclei *Phys. Rev.* C **51** 2798–880

[28] Zhang H H, Wang H L, Meng H Y, Liu M L and Ding B 2022 Impact of the Coriolis interaction on the potential landscape evolution across the nuclide chart: Systematic total-Routhian-surface calculations *Phys. Scr.* **97** 025303

[29] Yang Q, Wang H L, Chai Q Z and Liu M L 2015 Total Routhian surface calculations of triaxial or γ-soft properties in even-A N = 76 isotones with $54 \leqslant Z \leqslant 68$ *Chin. Phys.* C **39** 094102

[30] Yang Q, Wang H L, Liu M L and Xu F R 2016 Characteristics of collectivity along the yrast line in even−even tungsten isotopes *Phys. Rev.* C **94** 024310

[31] Yang J, Wang H L, Chai Q Z, Liu M L and Xu F R 2016 Evolution of shape and rotational structure in neutron-deficient $^{118-128}$Ba nuclei *Prog. Theor. Exp. Phys.* **2016** 063D03

[32] Chai Q Z, Zhao W J, Liu M L and Wang H L 2018 Calculation of multidimensional potential energy surfaces for even −even transuranium nuclei: Systematic investigation of the triaxiality effect on fission barrier *Chin. Phys.* C **42** 054101

[33] Wang H L, Liu M L, Xu F R and Feng C J 2012 Investigation of octupole effects in superheavy nuclei with improved potential-energy-surface calculations *Chin. Sci. Bull.* **57** 1761–4

[34] Wang H L, Chai Q Z, Jiang J G and Liu M L 2014 Rotational properties in even−even superheavy $^{254-258}$Rf nuclei based on total-Routhian-surface calculations *Chin. Phys.* C **38** 074101

[35] Chai Q Z, Zhao W J, Wang H L, Liu M L and Xu F R 2018 The triaxiality and Coriolis effects on the fission barrier in isovolumic nuclei with mass number A = 256 based on multidimensional total Routhian surface calculations *Prog. Theor. Exp. Phys.* **2018** 053D02

[36] Werner T R and Dudek J 1992 Shape coexistence effects of super- and hyperdeformed configurations in rotating nuclei with $58 \leqslant Z \leqslant 74$ *At. Data Nucl. Data Tables* **50** 179–267

[37] Dudek J, Herskind B, Nazarewicz W, Szymanski Z and Werner T R 1988 Pairing, temperature, and deformed-shell effects on the properties of superdeformed ^{152}Dy nucleus *Phys. Rev.* C **38** 940–52

[38] Myers W D and Swiatecki W J 1966 Nuclear masses and deformations *Nucl. Phys.* **81** 1–60

[39] Pomorski K and Dudek J 2003 Nuclear liquid-drop model and surface-curvature effects *Phys. Rev.* C **67** 044316

[40] Bolsterli M, Fiset E O, Nix J R and Norton J L 1972 New calculation of fission barriers for heavy and superheavy nuclei *Phys. Rev.* C **5** 1050–77

[41] Dudek J, Nazarewicz W and Werner T 1980 Discussion of the improved parametrisation of the Woods−Saxon potential for deformed nuclei *Nucl. Phys.* A **341** 253–68

[42] Bhagwat A, Vin¨as X, Centelles M, Schuk P and Wyss R 2012 Microscopic−macroscopic approach for binding energies with the Wigner−Kirkwood method. II. Deformed nuclei *Phys. Rev.* C **86** 044316

[43] Bohr A 1952 Quadrupole degree of freedom for the nuclear shape *Mat. Fys. Medd. K. Dan. Vidensk. Selsk.* **26** 1

[44] Bohr A and Mottelson B R 1998 *Nuclear Structure* vol 2 (Singapore: World Scientific)

[45] Meng H Y, Hao Y W, Wang H L and Liu M L 2018 Signature of yrast-state structure in even−even hafnium isotopes based on traditional total-Routhian-surface calculations and novel E-GOS curves *Prog. Theor. Exp. Phys.* **2018** 103D02

[46] Cwiok S, Dudek J, Nazarewicz W, Skalski J and Werner T 1987 Single-particle energies, wave functions, quadrupole moments and g-factions in an axially defformed Woods −Saxon potential with applications to the tow-center-type nuclear problems *Comp. Phys. Comm.* **46** 379–99

[47] Werner T R and Dudek J 1995 Shape coexistence effects of super- and hyperdeformed configurations in rotating nuclei II. nuclei with $42 \leqslant Z \leqslant 56$ and $74 \leqslant Z \leqslant 92$ *At. Data Nucl. Data Tables* **59** 1–181

[48] Nilsson S G, Tsang C F, Sobiczewski A, Szymański Z, Gustafson C, Lamm I L, Möller P and Nilsson B 1969 On the nuclear structure and stability of heavy and superheavy elements *Nucl. Phys.* A **131** 1–66

[49] Strutinsky V M and Ivanyuk F A 1975 A new definition of shell corrections to the liquid drop energy *Nucl. Phys.* A **255** 405–18

[50] Pomorski K 2004 Particle number conserving shell-correction method *Phys. Rev.* C **70** 044306

[51] Vertse T, Kruppa A T, Liotta R J, Nazarewicz W, Sandulescu N and Werner T R 1998 Shell corrections for finite depth potentials: particle continuum effects *Phys. Rev.* C **57** 3089–98

[52] Kruppa A T, Bender M, Nazarewicz W, Reinhard P-G, Vertse T and Cwiok S 2000 Shell corrections of superheavy nuclei in self-consistent calculations *Phys. Rev.* C **61** 034313

[53] Gaamouci A, Dedes I, Dudek J, Baran A, Benhamouda N, Curien D, Wang H L and Yang J 2021 Exotic toroidal and superdeformed configurations in light atomic nuclei: predictions using a mean-field Hamiltonian without parametric correlations *Phys. Rev.* C **103** 054311

[54] Pradhan H C, Nogami Y and Law J 1973 Study of approximations in the nuclear pairing-force problem *Nucl. Phys.* A **201** 357–68

[55] Satuła W, Wyss R and Magierski P 1994 The Lipkin−Nogami formalism for the cranked mean field *Nucl. Phys.* A **578** 45–61

[56] Xu F R, Satuła W and Wyss R 2000 Quadrupole pairing interaction and signature inversion *Nucl. Phys.* A **669** 119–34

[57] Möller P and Nix J R 1992 Nuclear pairing models *Nucl. Phys.* A **536** 20–60

[58] Meng H Y, Wang H L and Liu M L 2022 Landscape appreciation of systematic structure properties in even−even nuclei along the valley of stability *Phys. Rev.* C **105** 014329

[59] Pritychenko B, Birch M, Singh B and Horoi M 2016 Table of E2 transition probabilities from the first 2^+ states in even −even nuclei *At. Data Nucl. Data Tables* **107** 1–139

[60] Xu F R, Walker P M, Sheikh Ja A and Wyss R 1998 Multi-quasiparticle potential-energy surfaces *Phys. Lett.* B **435** 257–63

[61] Bengtsson T and Ragnarsson I 1985 Rotational bands and particle−hole excitations at very high spin *Nucl. Phys.* A **436** 14–82

[62] Möller P, Nix J R, Myers W D and Swiatecki W J 1995 Nuclear ground-state masses and deformations *At. Data Nucl. Data Tables* **59** 185–381

[63] Goriely S, Tondeur F and Pearson J M 2001 A Hartree−Fock nuclear masss table *At. Data Nucl. Data Tables* **77** 311–81

[64] Aboussir Y, Pearson J M, Dutta A K and Tondeur F 1995 Nulear mass formula via an approximation to the Hartree−Fock method *At. Data Nucl. Data Tables* **61** 127–76

[65] Dudek J, Nazarewicz W and Olanders P 1984 On the shape consistency in the deformed shell-model approach *Nucl. Phys.* A **420** 285–96

[66] Abusara H, Afanasjev A V and Ring P 2012 Fission barriers in covariant density functional theory: Extrapolation to superheavy nuclei *Phys. Rev.* C **85** 024314